Congruent Phase Behavior of a Binary Compound Crystal of Colloidal Spheres and Dimpled Cubes

Isabela Quintela Matos¹ and Fernando Escobedo^{1 a)}

¹School of Chem. and Biomolecular Engineering, Cornell University, Ithaca, New York 14853, USA.

a)Corresponding author: fe13@cornell.edu

Abstract.

Monte Carlo simulations were performed to study the phase behavior of equimolar mixtures of spheres and cubes having selective inter-species affinity. Such a selectivity was designed to promote the formation of the substitutionally ordered NaCl compound, the "C* phase", and to be driven not only by energetic bonds but also entropic bonds generated by dimples on the cube facets. Nestling of the spheres in the cube indentations can promote negative nonadditive mixing and increase the C* phase packing entropy. The focus is on congruent phase behavior wherein the C* phase directly melts into, and can be conveniently accessed from, the disordered state. A specialized thermodynamic integration scheme was used to trace the coexisting curves for varying values of the interspecies contact energy, ε^* , the relative indentation size, λ , and the sphere-to-cube size ratio, ζ . By starting from a known coexistence point with $\varepsilon^* > 0$ and $\lambda = 0$ (no indentation), it is found that increasing λ (at fixed ε^* and ζ) reduces the free-energy and pressure of the C* phase at coexistence, indicative of stronger entropic bonding. Remarkably, it is demonstrated that a purely athermal C* phase (i.e., with $\varepsilon^* = 0$) can be formed for $\lambda \ge 0.7$ and suitable choices of ζ . A metric of nonadditive (excess) volume of mixing is also suggested as an approximate predictor of athermal C* phase stability. The principles used to engineer selective entropic bonds and compounds with congruent melting

are expected to be applicable to other particle shapes and crystalline phases.

1

1. INTRODUCTION

Nanoparticles (NPs) can be arranged into different periodic structures with optical,¹ electronic,² and catalytic or mechanical^{3,4} properties that have potential applications in the development of materials for fuel cell membranes, solar photovoltaics, and carbon dioxide storage.⁵ Hence, engineering the self-assembly of these particles by tuning entropic and energetic interactions has become one of the central themes of recent investigations devoted to mapping the phase diagrams of NP mixtures.^{1,6-9} The implementation of energetic interactions usually includes electrostatic charges,^{1,7} grafted complementary DNA or DNA-like strands,^{8,10-13} and patchy or directional binding potentials.⁹ Likewise, entropic interactions can be engineered by leveraging, e.g., the preferential packing arrangements of NPs with polyhedral facets⁹ or with complementary-shapes.¹⁴

Considering the plethora of arrangements that can be produced based on NP building blocks and the chosen energetic interactions, a key challenge to address is to predict the conditions at which desirable phases can be formed. Many papers^{9,15–23} have reported on the phase behavior of pure-component convex and stoichiometric mixtures of polyhedral systems. Non-convex polyhedral NPs have also been studied, ^{14,18,24,25} but to a much lesser extent. Some non-convex particles which have already been synthesized experimentally include frame rings and cages, ^{26–28} curved and circular segments, ^{29,30} branched and non-convex polyhedra, ^{31–33} protruded and multicavity particles, ^{34,35} and dimpled spheres. ³⁶ Depending on the shape of the non-convexity, it is expected that materials containing such particles will exhibit distinct microstructures and associated thermophysical properties. For example, particles with protrusions do not typically pack densely, which can impact mechanical strength, ³⁷ while particles with non-convex or

complementary shapes can assemble into porous ordered microstructures. ¹⁴ Specifically, the effect of the entropic lock-and-key attraction of shape-complementary particles designed to generate nonadditive mixing can lead to the formation of lattices that favor states of high packing entropy. ^{38–40} Despite their promise, non-convex particle modeling with analytical models presents some challenges associated with slow global ergodic equilibration, representation of particle geometry, and the development of overlap algorithms to represent excluded-volume interactions in hard-core systems. ¹⁴

Nonadditive mixing occurs when the volume of the mixed state is either larger (positive) or smaller (negative) than the sum of the individual components' volumes. Nonadditive mixing can occur, e.g., when the characteristic length "\sigma" of contact between two particles A and B differs from the arithmetic average of the characteristic contact lengths for A pairs and B pairs (σ_{AB} = $((\sigma_{AA} + \sigma_{BB})/2 + \Delta)$; i.e., for spherical sites, it deviates from the so-called Lorentz's additivity rule. One of the first models developed using this property was the Widom-Rowlinson binary mixture of spheres, 41, which produced fluid-vapor and fluid-fluid transitions when like species are repulsive and unlike species are non-interacting ($\Delta > 0$). In the Asakura-Oosawa model⁴² for the depletion effect of polymeric depletants on large colloidal particles, the polymer coils only exclude volume to the colloids but not to other polymer coils. Similarly, the nonadditive Holland model⁴³ has been used to model the chemisorption of gases in the crystal phase.⁴³ A key feature of these models is that the nonadditivity parameter (Δ) induces an entropy-driven demixing phase transition at high densities. 44 Note, however, that a solid-fluid mixture can exhibit reentrant mixing with Δ for a small range of Δ .⁴⁵ More recently, Kumar and Molinero introduced a model that combines a positive value of Δ with a high cross interaction energy parameter ($\varepsilon_{AB}/\varepsilon_{AA}>1$) between two spherical particles, which lead to the formation of a wide variety of novel liquid-crystals. 46

NP-based stoichiometric crystals or compounds constitute a novel class of materials where the effects of nonadditivity could be very significant. These materials are analogous to salts and intermetallic alloys and also expected to have properties that are not merely an interpolation of the features of their components. 9 Such compounds are most conveniently attained by the selective energetic attraction between unlike NP pairs. That is the reason why several experimental studies have focused on achieving such selectivity by grafting the NPs with complementary DNAstrands.^{8,13,47} In one of these studies,⁴⁷ mixtures of spheres and either cubes or octahedra formed crystals with a NaCl and CsCl lattices, respectively. Partially motivated by these observations, our group proposed a general rule to maximize the thermodynamic stability of stoichiometric colloidal mixtures, and applied it to the cases of spheres + cubes and spheres + octahedra; the rules provide specific prescriptions for optimizing the components' relative size and cross interaction energetic parameter. 9,17 Another takeaway from this study was that the formation of the NaCl lattice only happened with a strong enough inter-species attraction parameter of the directional potential, a selectivity effect experimentally achievable with complementary DNA strands. This energetic directional attraction between cubes and spheres is necessary to form a compound phase since mixing entropy favors the formation of substitutionally disordered solid solutions.¹⁷

The formation of substitutionally ordered compounds is potentially achievable in athermal systems; for example, binary hard-spheres of specific size ratios have been predicted to form different types of compounds. However, additive hard-sphere mixtures do not exhibit congruent melting/freezing (where liquid and solid have the same composition), which would make very difficult the usual experimental route of crystallizing such compounds directly from the isotropic state. Note that congruent phase behavior is the second most common among binary organic mixtures. Pertinently, it has been proven that nonadditive binary hard-sphere mixtures of can form

compound solids that do exhibit congruent melting/freezing. In that study, however, nonadditivity was enacted by artificially imposing a $\Delta < 0$ in the Lorentz mixing rule, an attribute that is highly non-trivial to achieve with realistic entropic interactions alone.

Because inter-species selective attraction can favor or be necessary to form binary compound phases and to have congruent melting/freezing, we use the flat cubes + spheres system studied in Ref. [9] as a starting point, and then introduce entropic bonds by making the cubes non-convex via indentations complementary to the spheres, as illustrated in Figure 1. Such indentations or dimples allow the cube-sphere contact distance to be closer than what would be expected from the additivity of cube-cube or sphere-sphere contact distances, hence generating a negative nonadditivity ($\Delta < 0$). By modeling the phase behavior of the mixture of spheres and non-convex cubes, we aim to study the effect of the size of the dents; i.e., the non-convexity ratio (λ) of the cubes, on the formation and stabilization of the compound crystal phase, which is henceforth denoted as the C* phase. λ is an experimentally attainable and tunable feature, which is also easy to envision and model geometrically. This model will also allow us to address a fundamental question that motivated this study: Can the underlying lock-and-key effect create a strong enough entropic attraction to access the crystal phase from the isotropic phase (congruent behavior) in the absence of energetic attractions?

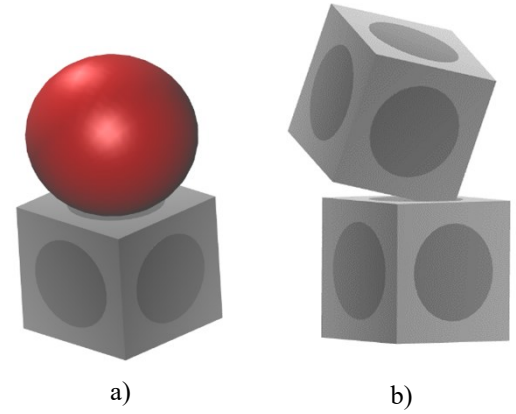


Figure 1: Representation of nonadditive mixtures of a) spheres + cube and b) cube + cube

2. COMPUTATIONAL METHODS

2.1. System and force field

The system used here of non-convex cubes of side a and spheres of diameter σ aims to provide a coarse-grained representation of preferential inter-species interactions. Following the baseline system of Ref. [9], we model the interactions between like particles (sphere-sphere or cube-cube) to be entirely repulsive. In contrast, the interactions between unlike particles follow a simplified squared-well like potential:

$$U_{11} = U_{22} = \begin{cases} \infty, & \text{if overlap} \\ 0, & \text{otherwise} \end{cases} \quad U_{12} = \begin{cases} \infty, & \text{if overlap} \\ -\varepsilon^* kT, & r \le r_c, \delta \le 0.8 \frac{a}{2} \end{cases} \quad (1)$$

Here, r is the distance between the particle centers, δ is the distance between the sphere center and the vector pointing out from the facet center and normal to it (see Figure 2 (a)). δ is set to be 40% of the cube side, so it favors sphere-polyhedral facet contact instead of sphere-polyhedral edge contact. The cutoff distance (r_c) is set to limit the range of the attraction energy between the

sphere and cube facet. By limiting the attraction of spheres and cubes to only occur over a limited range of interparticle distances and high facet alignment, we can enact an energetic contact bond analogous to that from multiple hydrogen bonds formed during DNA hybridization. The main difference between the model used in this paper and that in our previous works^{9,17} is that the parameters r_c and the criteria for overlap are now dependent on the diameter of the spherical indentations (d_h) depicted in the diagram of Figure 2 (b):

$$r_c = d_{min} + 0.15a \tag{2}$$

$$d_{min} = \frac{a}{2} + \frac{1}{2} \sqrt{\sigma^2 - d_h^2} \tag{3}$$

$$\delta_{max} = \frac{1}{2} \left[d_h - \sqrt{\sigma^2 - (2d - a)^2} \right] \tag{4}$$

The δ_{max} of Eq. (4) is the maximum δ that a nested sphere can have without overlapping with the edge of the cube, as shown in Figure 2 (a). The basis for the overlap criteria was the Arvo algorithm.⁵¹ The criterion for overlap avoidance is that the distance d defined in Figure 2 (b) should be larger than the d_{min} value prescribed in Eq. (3).

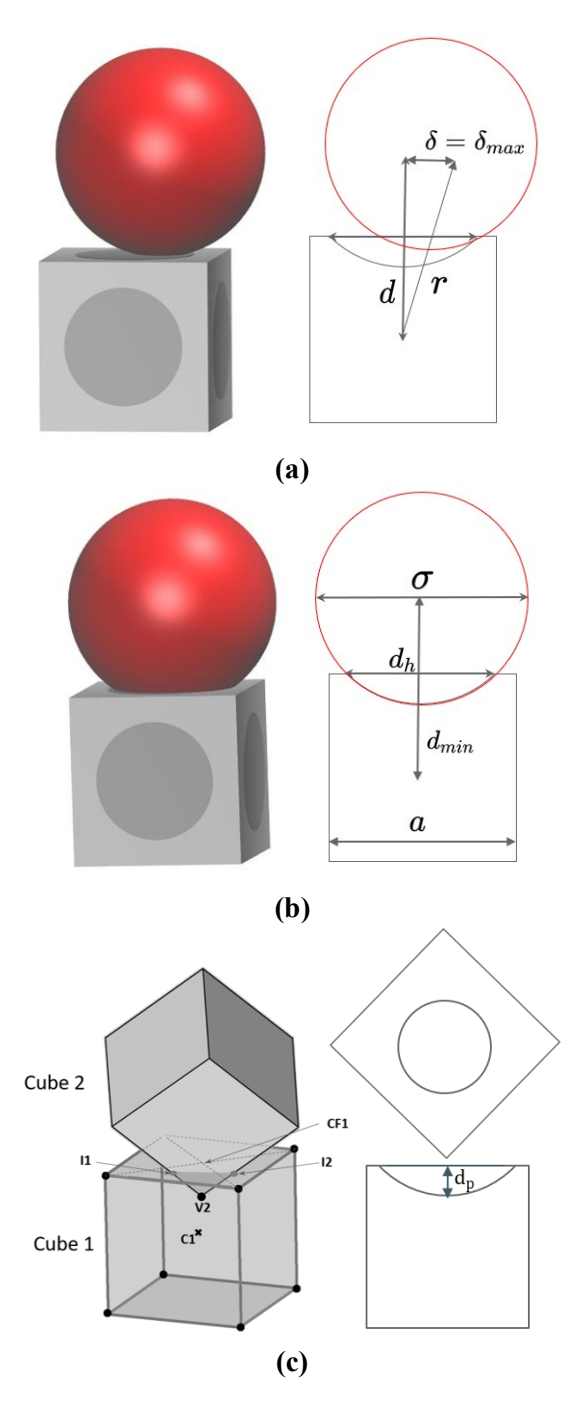


Figure 2: Schematics of the system geometry and criteria used to determine overlap for (a)-(b) non-convex cube +sphere pair and (c) non-convex cube + non-convex cube pair.

The criterion to detect overlaps between non-convex cubes was based on the separating axes theorem.⁵² We implemented some modifications on the standard cube-cube overlap algorithm to allow the edges of a cube to penetrate the spherical indentations of another cube, such as the case

illustrated in Figure 2 (c). For this purpose, we followed three steps: (i) Calculate the distance between the center of cube 1 (C1) and all the vertices of cube 2. (ii) Store the vertex of cube 2 (V2) that is closest to C1 (iii) Check if the distance between the closest facet of cube 1 (F1) and V2 is smaller than the depth of the concavity (d_p) , see Figure 2 (c). (iv) If this criterion is satisfied, then we check if the distances between the intersection points of cube 2 with the facets of cube 1 (e.g., I1 and I2) and CF1 are larger than the indentation radius (i.e., $> \frac{1}{2}d_h$). Another important geometrical feature of our system is the ratio ζ between the characteristic lengths of the spheres and cubes in the compound phase. It is defined as:

$$\zeta = \sigma/a \tag{5}$$

The spheres need to be slightly bigger than the cubes so that each sphere could simultaneously nest with four cubes in the NaCl (C*) phase. The initial ratio chosen for the analysis was $\zeta = 1.23$, a value that was found to provide maximum stability of the substitutionally disordered crystal phase of spheres and convex cubes.¹⁵ The geometrical parameter used to define the non-convexity ratio of the cubes is:

$$\lambda = d_h/a \tag{6}$$

which is used as varying parameter to map the phase diagram of the mixture (playing a role akin to that of parameter ζ for the system with convex cubes in Ref. [9]). These parameters are defined in dimensionless form to facilitate the thermodynamic integration calculations. As a guide for the following sections, we summarize our system's parameters in Table 1.

Table1: Design parameters for the spheres + dimpled cubes system.

Symbol	Meaning [Equation #]	Range explored
λ	Ratio of indentation diameter to sphere	0.0 - 1.0
	diameter [Eq. (6)]	
ζ	Ratio of sphere diameter to cube edge	1.19-1.36
	[Eq. (5)]	
$arepsilon^*$	Contact energy between cubes and	0.0 - 1.0
	spheres [Eq. (1)]	

We propose as an approximate metric for the nonadditivity parameter, Δv , a reduced excess volume:

$$\Delta v = v(C^*)/v(\text{premix}) - 1 \tag{7}$$

Where $v(C^*)$ is the volume of the C^* phase at infinite pressure (densest state), and v(premix) is the volume of pure cubes and pure spheres before mixing happens at the equimolar composition and densest state. For $\Delta v < 0$, we have negative volume of mixing. Δv has the advantage of being equally applicable to isotropic and anisotropic NP shapes or potentials.

Figure 3 shows how Δv varies with λ . It is clear that relatively large values of λ are needed to attain a negative nonadditivity in comparing the C* with the crystal states of pure cubes and spheres; e.g., for $\zeta = 1.23$ we would require $\lambda > 0.8$. While any indentation size ($\lambda > 0$) does create an entropic sphere-cube facet bonding effect, a large λ , enough to generate negative nonadditivity, would be expected to be crucial to stabilize the C* phase in the absence of any energetic bonding (i.e., for $\varepsilon^* = 0$); this prediction will be revisited in the Results Section.

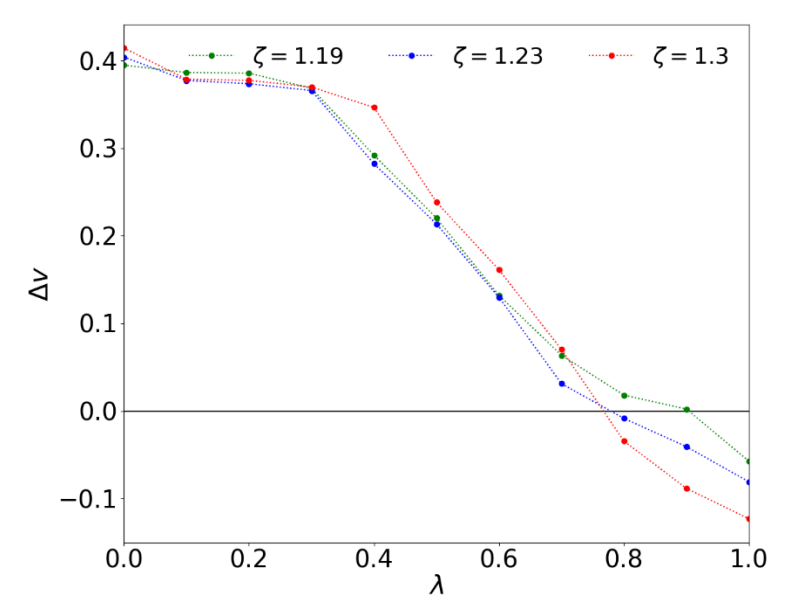


Figure 3: Nonadditive mixing parameter as defined in Eq. (7) as a function of λ for three different values of ζ . Error estimates from statistical fluctuations are smaller than the symbols sizes.

2.2. Free energy methods

We aim to trace coexistence lines, i.e., the thermodynamic properties of the coexisting C^* phase and the isotropic phase (I) as a function of λ [in Eq. (6)], ζ [in Eq. (5)], and ε^* [in Eq. (1)]. For notational brevity, these model parameters, which are part of the system Hamiltonian, will be denoted by the symbol f in the equations below ($f = \lambda$, ζ , or ε^*). In our system, we are fixing the number of particles (N), reciprocal temperature ($\beta = 1/kT$), pressure (P), and composition since we are only looking into the (equimolar) stoichiometric mixture. Hence, the free energy (ϕ) can be written as a function of the isobaric-isothermal configurational partition function:

$$N\phi = -\ln \sum \exp[-\beta U(f) - \beta PV]$$
 (8)

where U is configurational energy, and V is volume. The relation between changes in f and P at constant β is given by the thermodynamic equation for the intensive dimensionless free energy ϕ :

$$d\phi = zdf + vdp \tag{9}$$

where $p = \beta P$, $v = (\partial \phi / \partial \beta P)_{f,\beta} = V/N$, and $z = (\partial \phi / \partial f)_{\beta P,\beta}$. The derivative z is evaluated in simulation using a finite perturbation approximation:

$$z \approx -\frac{1}{N\delta f} \ln \frac{\sum \exp[-\beta U(f + \delta f) - \beta PV]}{\sum \exp[-\beta U(f) - \beta PV]}$$
$$= -\frac{1}{N\delta f} \ln \langle \exp[-\beta U(f + \delta f) + \beta U(f)] \rangle \tag{10}$$

Here, δf is a small perturbation on the control variable f. If we can decouple f from U (i.e., $\beta U(f) = fU'$), as for the case when $f = \varepsilon^*$, Eq. (10) can be written as:

$$z \approx \frac{\langle U' \rangle}{N} = u' \tag{11}$$

Derivations of these approximations can be found in reference [9]. With equations (10) or (11) showing how the coefficients of Eq. (9) are found in simulation, we can stepwise integrate Eq. (9) numerically to evaluate changes in ϕ . To target the phase I-C* phase coexistence conditions, one then writes Eq. (8) separately for both the C* and I phases and then combine them to make sure that, for identical values (and changes) in f and p the free-energy ϕ is identical in both phases. Among the methods available to estimate free-energy changes, we adopt the Free-Energy Extrapolation (FENEX)¹⁵ method as it combines the robustness of Gibbs-Duhem integration method⁵³ with the ability to estimate free energies of histogram-based methods^{54–56} by using polynomial models to extrapolate the free energy. As with any integration method, we need to start our integration from a known state. Since our previous studies explored the phase behavior of convex (flat-facet) cubes, we started the integrations from the coexistence states found in the reference paper.⁹ In Reference [9], the coexistence pressure between the C* and I phases was mapped as a function of a dimensionless energy parameter ε^* for convex cubes; i.e., for $\lambda = 0$.

To mitigate possible finite-integration step errors associated with the methodology, we redid the integration in reference [9] to have finer integration steps and hence a more accurate coexistence curve. After this calculation, we picked a point on this curve to carry out integrations for varying degree of indentation λ . We obtained the coexistence lines for different values of λ (using points generated in the previous step) by performing the integration over ε^* . The integrations stopped at the point in which the obtained coexistence pressure resulted in the melting or transformation of the C* phase. Finally, we fixed ε^* and λ to integrate over the variable ζ . As can be seen, three types of integrations were performed:

(i) For the integrations over ε^* at fixed λ and ζ , z is given in Eq. (11) and Eq. (9) becomes:

$$d\phi = u'd\varepsilon^* + vdp \tag{12}$$

The simulations on both the I and C* are carried out at fixed values of d_h (or λ), ε^* , and p, so that the averages and covariances of the potential energy (u') and specific volume (v) are stored as these are needed for the FENEX calculations.

(ii) For integrations over λ at fixed ε^* and ζ , z needs to be evaluated from Eq. (10) due to its non-linear relationship to the Hamiltonian of our system. Here, we are fixing the cube edge (a) and changing the non-convexity ratio (λ), so the equation to integrate has the following form:

$$d\phi = z_1 d\lambda + v dp \tag{13}$$

During the concurrent simulations for both phases, the values of p, ε^* , and λ remain fixed. However, small virtual perturbations ($\delta\lambda$ = -0.00005) on λ are probed (but not enacted) to calculate z via Eq. (10), whose value and those of v and their covariances are evaluated. Integrations over ζ at fixed ε^* and λ follow the same procedure. The difference is that we are fixing the cube edge

(a) and changing the sphere diameter (σ), and the perturbations probed are positive ($\delta \zeta = 0.00005$). The equation to integrate is:

$$d\phi = z_2 d\sigma + v dp \tag{14}$$

Details of how the FENEX method calculates the next coexistence point on the integration from the polynomial models are explained elsewhere. ^{9,15} To check the consistency of the method and obtain an error estimate for the pressure and free-energy values, we repeated the same integration over f in two different directions (e.g., first on the direction of increasing λ and then in the direction of decreasing λ). The results from these two integrations at each step were averaged to report coexistence p and ϕ values and subtracted to estimate the integration method's error.

We note that alternative methods could also be used to find the sought-after I-C* phase coexistence states such as interfacial simulations ^{16,57,58} (with both phases present in a single box) and gradual decompression/compression or heating/cooling runs that directly detect when one phase transforms into the other. ^{16,18} Compared to Gibbs-Duhem type on integration methods for mixtures, ^{15,54} however, the former method entails multiple trial-and-error exploratory runs and stronger finite-size effects, while the latter method is prone to very large hysteretic effects.

2.3. Simulation details

All simulations on the C* and I phases were carried using the Monte Carlo (MC) method in the isothermal-isobaric ensemble (N_1N_2PT). The initial configuration is a perfect NaCl lattice for the C* phase and a pre-equilibrated isotropic box for the I phase. The ratio of cubes to spheres (N_1 and N_2) is fixed to 1 and the total number of particles N = 1728 was also chosen to fit the NaCl lattice symmetry in a cubic box. Henceforth, all the simulation results will be reported in the following

reduced units: $\varepsilon^* = \varepsilon \beta$, $v = V/NL^3$, $p = \beta PL^3$, and $\rho = NL^3/V$, where the reciprocal temperature β is set to 1 and L is half the cube edge length $(\alpha/2)$.

The coexistence pressure obtained from the FENEX method was used on the NPT simulations of the C* and I phases. These simulations for every point along the estimated coexistence line consisted of 3×10^6 MC cycles, in which the first 10^6 were equilibration cycles. Additional cycles were carried out if there were large volume fluctuations during the simulation. Each cycle consisted of N translation moves, N rotational moves (performed only on the cubes), N/5 swap moves, and 3 volumes attempts. To calculate z in Eq. (10) when integrating over λ or ζ , one virtual move per MC cycle was also conducted to change the size of indentation or the sphere, respectively. Upon completing the simulations, we calculated a series of order parameters (OP) on the resulting structures to characterize the crystalline phase. The first OP used was the average cubatic orientational order parameter P_4 : ⁵⁹

$$P_4 = \frac{1}{14N_2} \sum_{ij} 35 \left| \mathbf{u}_{ij} \cdot \mathbf{n} \right|^4 - 30 \left| \mathbf{u}_{ij} \cdot \mathbf{n} \right|^2 + 3$$
 (15)

where N_2 is the number of cubes, \mathbf{u}_{ij} is the unit vector of particle i along its axis j, and \mathbf{n} is the unit vector that maximizes P_4 . We also calculated a short-range compositional order parameter (SROP) to determine if the structure exhibited the expected substitutional order of the compound. For the C* phase studied here, every sphere should have cubes as its six nearest neighbors and vice versa. Hence, we define an average SROP for our system as:⁶⁰

$$SROP = \frac{1}{N} \sum_{i} \frac{t_i}{6}$$
 (16)

where t_i is the number of different-species neighbors of particle i among its six closest neighbors.

2.4. Overall Simulation Strategy

Figure 4 depicts the $(\zeta, \lambda, \varepsilon^*)$ search space where our main goal is to identify athermal I-C* congruent phase coexistence states, shown as a closed gray area on the ζ - λ plane $(\varepsilon^* = 0)$. Recalling that such athermal states are unattainable for the flat-cube case, our strategy to find them, as per the methodology described above, can be summarized by the 3 steps listed below and illustrated in Fig. 4:

Step 1 (green line in Fig. 4). Carry out a FENEX integration over λ at fixed $\varepsilon^* = \varepsilon_0^*$ and $\zeta = \zeta_0$, from $\lambda = \lambda_0 = 0$ (flat-faced cubes) to $\lambda = 1$. We have to start from $\lambda_0 = 0$ with energetic interactions ($|\varepsilon^*| > 0$) since those conditions are the only known I-C* phase coexisting states which can be used to initiate any new FENEX integration. The initial point is depicted by a black circle in Fig. 4 and corresponds to $\varepsilon_0^* = 0.55$, $\zeta_0 = 1.23$, and $\lambda_0 = 0$.

Step 2 (blue lines in Fig. 4). Integrate over ε^* at fixed λ and $\zeta = \zeta_0$, from $\varepsilon^* = \varepsilon_0^*$ to $\varepsilon^* \to 0$ or until I-C* phase coexistence is maintained. These integrations were performed for a range of different λ values to detect conditions when the athermal I-C* phase coexistence was attainable.

Step 3 (red lines in Fig 4). Perform integrations over ζ at fixed λ and ε^* and integrations over ε^* at fixed λ and ζ , to identify other combinations of λ and ζ that result in an athermal C* phase. Crossing the stability boundary of I-C* phase coexistence could manifest here by either phase I or C* switching into a different phase.

Note that integrations along a single variable (keeping the other two parameters constant) also allow us to elucidate the effect of that variable on phase stability and microstructure; i.e., to isolate the effect of indentation (in step 1), strength of energetic contacts (in step 2) and relative sphere to cube sizes (in step 3). Note also that for any (λ, ζ) combination where athermal I-C* states occur,

there is an associated range of pressures (i.e., thermodynamic states) which are not visible in Fig. 4.

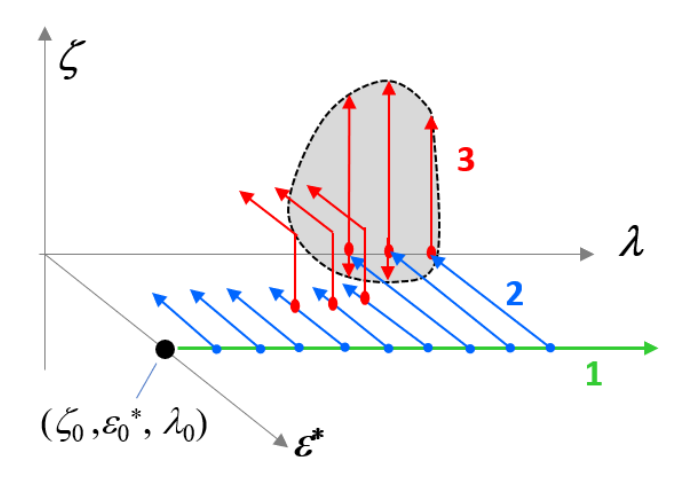


Figure 4: Depiction of the $(\zeta, \lambda, \varepsilon^*)$ space to explore and the ζ - λ region (shaded in gray) where athermal I-C* phase behavior occurs. Steps 1 (green arrow), 2 (blue arrows), and 3 (red arrows) correspond to sequential FENEX integrations aimed to locate states in the gray region.

3. RESULTS

3.1. Phase behavior for non-convex cubes at fixed ζ

The initial point to start the analysis of the effect of the non-convexity ratio on the phase behavior was chosen from the integration for the flat-faced cubes ($\lambda=0$). These I-C* coexistence conditions correspond to $\varepsilon^*=0.55$, $\zeta=1.23$, and p=0.948. This specific point of ε^* was chosen because the NaCl lattice order characteristics are well maintained. It was shown previously that the C* phase for a system of convex cubes and spheres is not stable for $\varepsilon^*<0.5$. By keeping ε^* and ζ constant and integrating Eq. (13) over λ , we obtained the coexistence curve of Figure 5. The error bars for the free-energies and pressures in Figure 5 were calculated as described in Section 2.2. As expected, the decrease in the free-energy at coexistence with the relative size of the cube indentation, λ , shows the strengthening of the entropic attraction generated by the more

complementary sphere-cube nesting interactions, which favors the realization of the C* phase. After $\lambda = 0.8$, the coexistence pressure seems to stabilize. As a check to the stability of the C* phase along this I-C* phase coexistence pressure curve, we calculated the extent of the alignment of the cubes using the average cubatic orientational order parameter P_4^{59} (with standard errors estimated from statistical fluctuation around the average values).

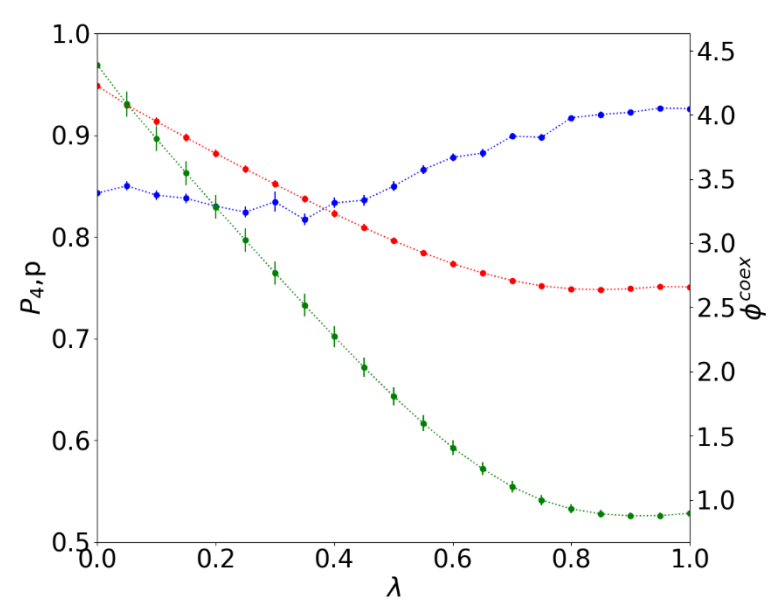


Figure 5: Reduced I-C* phase coexistence pressure (p) (red), orientational order parameter (P_4) (blue), and free energy at coexistence (ϕ^{coex}) (green) of the C* phase as a function of the non-convexity ratio (λ) for $\varepsilon^* = 0.55$. Errors were smaller than 0.1 for ϕ^{coex} and smaller than 0.005 for p and P_4 .

Following the strategy laid out in Sec. 2.4, we carried integrations of Eq. (12) to get the coexistence pressure curves as a function of λ for different ε^* values as shown in Figure 6(a). These curves have the same behavior as the one in Figure 5, with the coexistence pressure decreasing with increasing λ for up to $\lambda \approx 0.8$ and plateauing thereafter. The free energy at coexistence also followed a similar trend (results not shown). The minimum value of ε^* for which the C* does not melt (ε^* near 0.5) remains almost unchanged for $\lambda < 0.5$, and finally reaches $\varepsilon^* = 0$ for $\lambda = 0.9$. This region where the C* is stable can been seen in Figure 6 (b). These results indicate that cubes

with a spherical indentation diameter of greater than 90% of their edge-length and sphere/cube ratio of $\zeta=1.23$ create a strong enough directional bond between the cubes and the spheres to result in a congruent I-C* phase behavior, even in the absence of any energetic attraction; i.e., a purely athermal system. These results are remarkably consistent with the predictions of Figure 4, which pointed to $\lambda>0.8$ (for $\zeta=1.23$) as the necessary condition to generate a negative nonadditive mixing and hence large enough gains in packing entropy to drive, by itself, the preferential nesting of spheres in cube dimples.

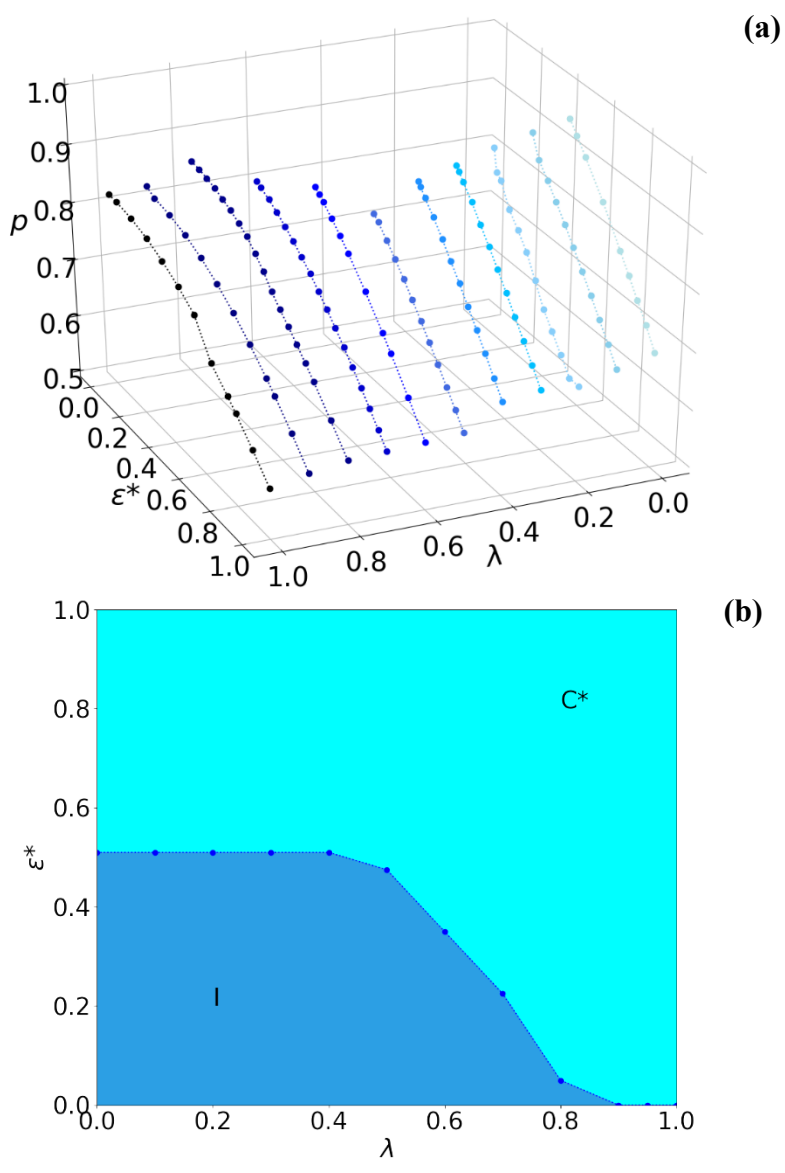


Figure 6: (a) I-C* coexistence pressure (p) as a function of inter-species energy parameter ε^* and non-convexity ratio (λ) . (b) Minimum value of ε^* capable of stabilizing the C* phase for different values of λ for $\zeta = 1.23$.

We carried out a structural and visual analysis to characterize the influence of the indentation on the C* phase for the minimum values ε^* of Fig. 6(b). First, we calculated the structural factor S(k) of all particles to check the maintenance of translational order in the form of the periodic patterns. Figure 7 shows selected snapshots and their corresponding projections of S(k) on the x-y (100 crystal) plane which confirm the conservation of the expected crystalline structure, even

for ε^* close or equal to zero. Additional snapshots for other λ , ε^* values are available in the supplementary information. Figure 8 shows the average P_4 of the cubes and the average SROP order parameters (including the packing fraction η for reference) for these minimum ε^* boundary points, further confirming that orientational and compositional ordering of the C* phase is maintained. The increase in both the SROP and P_4 parameters with λ , even in the absence of energetic interactions, is indicative of the growing strength of the entropic bonds enacted by the larger/deeper indentations. For the I phase, the SROP fluctuated closely around 0.5 and the P_4 values were almost zero for all conditions examined.

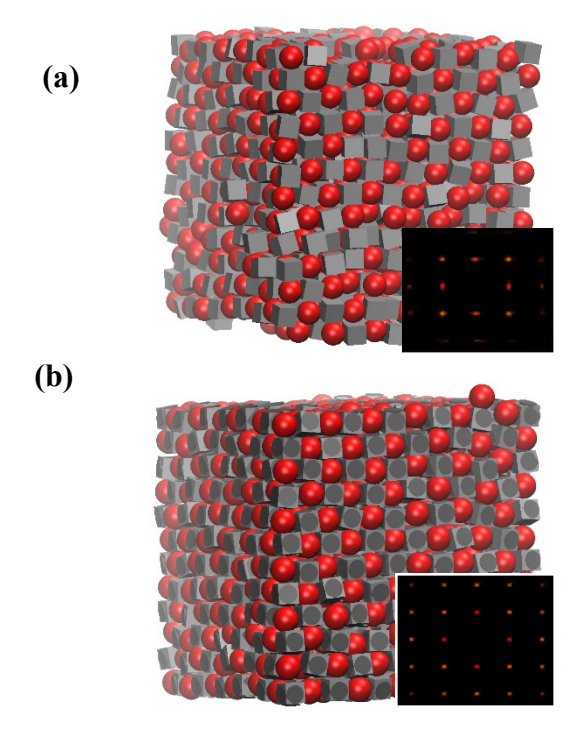


Figure 7: Representative snapshots of the C* phase and (as insets) projection of the structure factor S(k) on the x-y plane at phase coexistence for (a) $\lambda = 0$ and $\varepsilon^* = 0.51$ (b) $\lambda = 0.9$ and $\varepsilon^* = 0$. The latter exhibits stronger signals of positional and substitutional ordering.

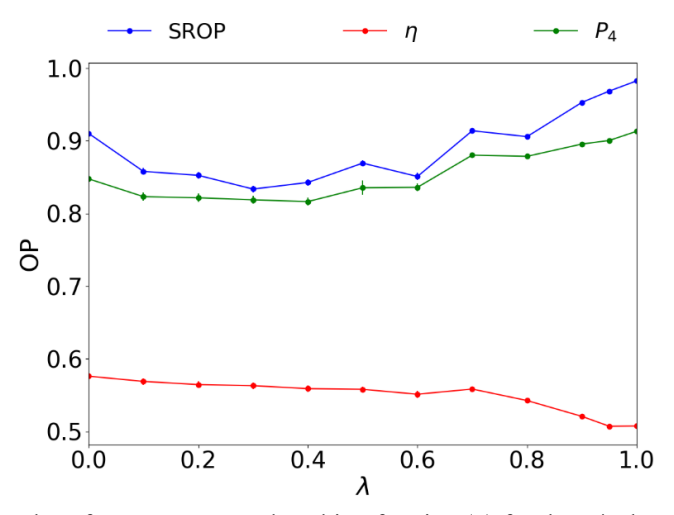


Figure 8: Order parameter values for SROP, P_4 , and packing fraction (η) for the C* phase at its low- ε * stability limit corresponding to each λ . Standard errors for the average order parameters were smaller than 0.01.

3.2. Combine effect of ζ and λ on I-C* phase behavior

Using the results of Section 3.1 as initial I-C* phase coexistence points, we integrated over ζ to find if other combinations of λ and ζ would stabilize the athermal C* phase, as explained in Section 2.4. We started with $\lambda=0.8$ since the minimum ε^* was already close to zero. The integration resulted in a value of $\zeta=1.26$ as the minimum value for which athermal I-C* equilibrium is possible. Figure 9 shows this stability region of the C* and the I-C* coexistence pressures. The same procedure was repeated for $\lambda=0.7$, and we found the correspondent minimum value of ζ to be equal to 1.30 (see Figure 10). The error bars in the pressures were estimated as described in Sec. 2.2. Note that as illustrated by red lines in Fig. 2, different integration paths were used to get the points (and respective errors) in Figure 9 (b) and 10 (b). As an example, we started from the point $\zeta=1.23$, $\varepsilon^*=0.1$, $\lambda=0.8$ and integrated first over ζ and then over ε^* . The resulting point $\zeta=1.26$, $\lambda=0.8$, $\varepsilon^*=0$ was then used as the starting point for the new integration over ζ . We also performed integrations in the direction of decreasing ζ until a value of 1.19, but they did not result in a smaller value of ε^* as the terminal point for the I-C* phase

equilibrium. This may happen because smaller spheres allow an increased contact among neighboring cubes, and edge-concave region contacts (see Figure 2 (b)) tend to favor the I phase. Also, the nonadditive mixing is not geometrically favorable for smaller spheres, as seen in Figure 3. The fact that the smallest λ at which the athermal C* phase stabilizes is $\lambda = 0.9$ for $\zeta = 1.23$ but only $\lambda = 0.7$ (a smaller cavity) for $\zeta = 1.30$ is consistent with the curves in Fig. 3 that show that the negative mixing effect is stronger for $\zeta = 1.30$.

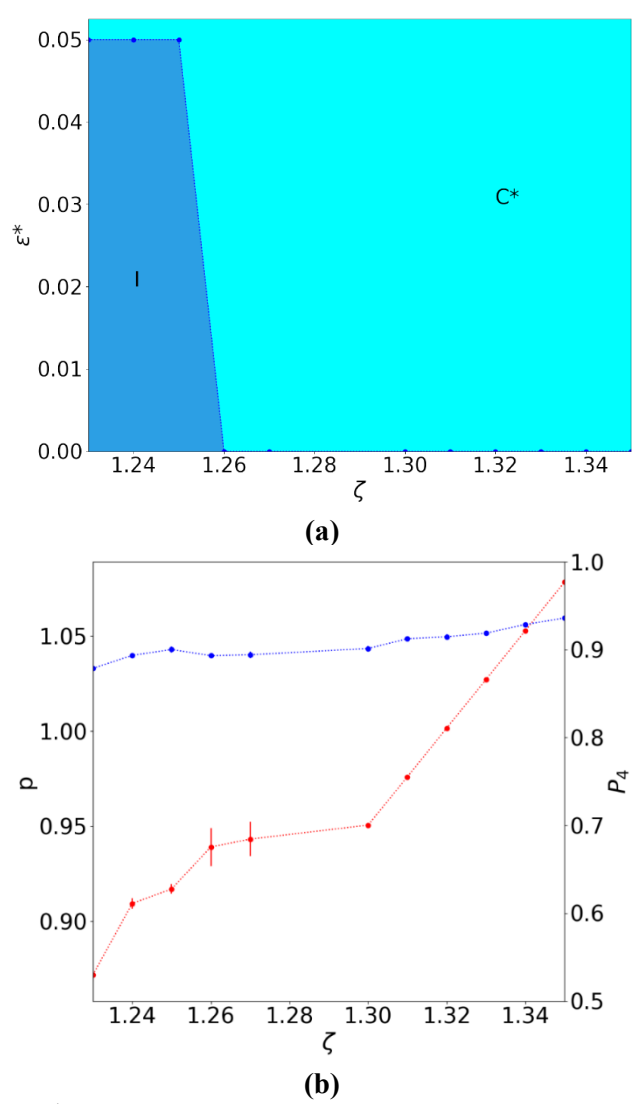


Figure 9: (a) Minimum value of ε^* capable of stabilizing the crystal phase for $\lambda = 0.8$ as a function of ζ . (b) I-C* coexistence pressure (p) (red) and P_4 (blue) vs. ζ for the points in (a). Estimated errors in p were smaller than 0.01, and standard errors in P_4 were ~ 0.003 .

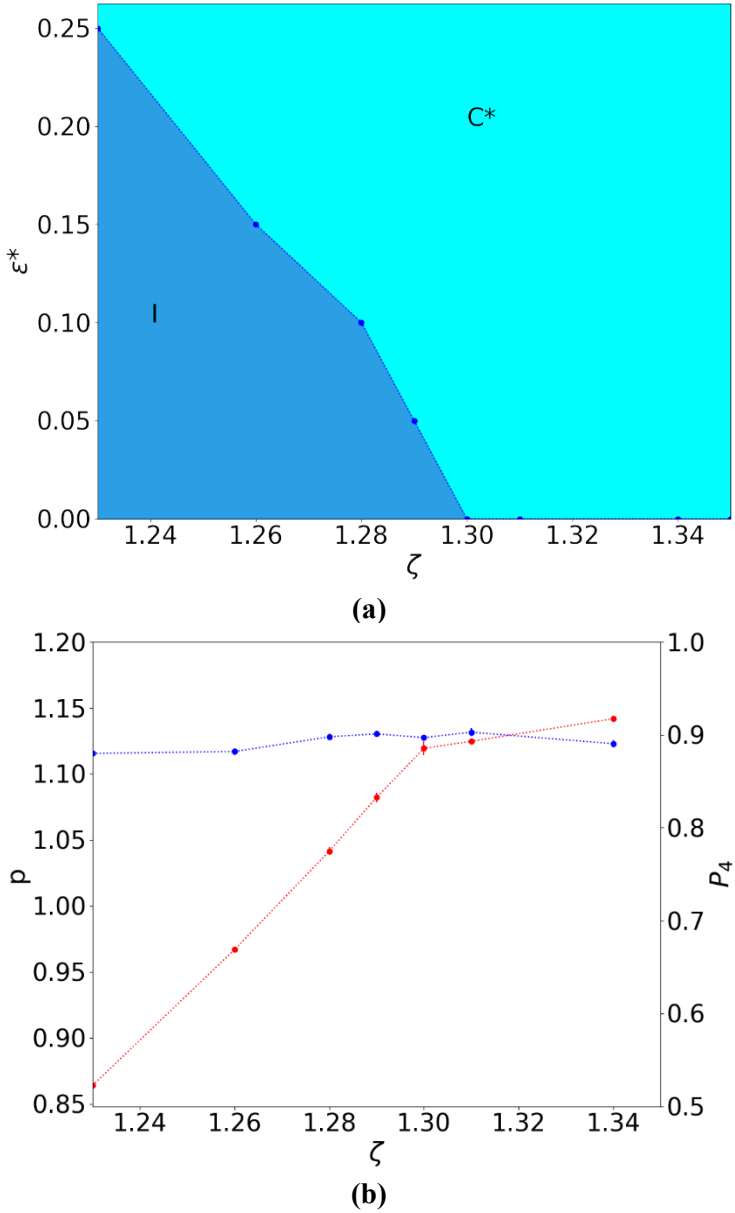


Figure 10: (a) Minimum value of ε^* capable of stabilizing the crystal phase for $\lambda = 0.7$ as a function of ζ . (b) I-C* coexistence pressure (p) (red) and P_4 (blue) vs. ζ for the points in (a). Errors in p estimated to be ~ 0.005 , and standard errors in P_4 to be ~ 0.004 .

Besides the plots of P_4 in Figures 9(b) and 10(b) that check the persistence of orientational order of the cubes, we also calculated the S(k) to confirm the translational order of the athermal C* phases. In Figure S.2, we show sample S(k) plots as insets for representative snapshots. Since the athermal I-C* phase transition was attained for ζ =1.23, these conditions were used as starting

point for the integrations over ζ for $\lambda = 0.9$ and $\lambda = 1.0$ at $\varepsilon^* = 0$. These pressure- ζ phase diagrams are shown in the supplementary information.

Figure 11 shows the relative free-energy of the athermal C* phase, \mathscr{C}^{oex} (at the I-C* athermal coexistence boundary) for several λ values in the [0.7-1.0] range. Such \mathscr{C}^{oex} values are readily accessible from the FENEX calculation. Following the optimization rule demonstrated in Ref. [9], lower \mathscr{C}^{oex} values signal a more stable C* phase. Accordingly, it is clear that for a given λ value, increasing ζ tends to lower the stability of the C* phase, a result consistent with the notion that a larger ζ means that a smaller portion of the sphere can nestle in the fixed-sized cube dimple, creating a weaker entropic bond. This trend also aligns with the corresponding trend of coexisting pressures seen in Figures 9 and 10 (with higher p needed to accentuate the pressure-volume contribution to the free-energy associated with the negative nonadditive mixing in the C* phase). Moreover, Figure 11 shows that for a given ζ , the larger the cavity (bigger λ) the lower the free energy and hence the better the system is in stabilizing the C* phase.

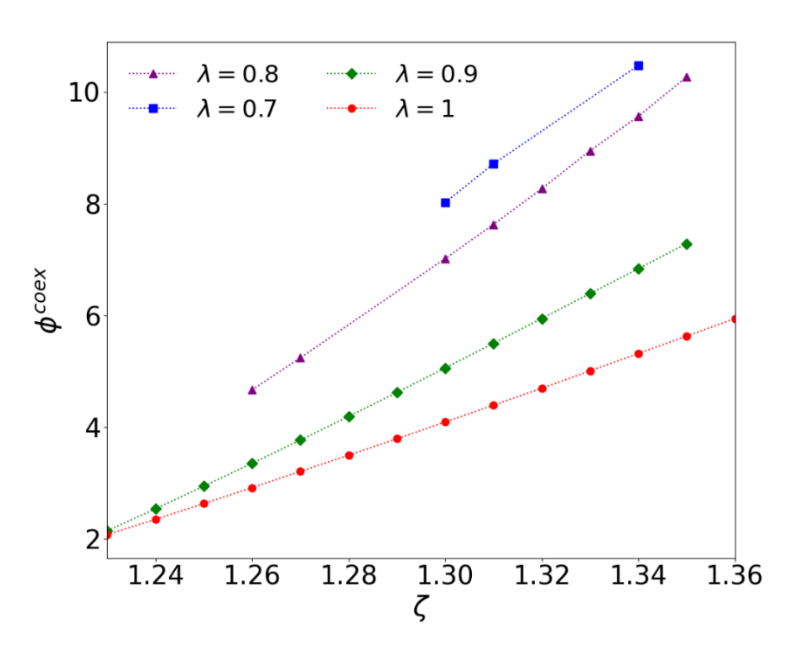


Figure 11: Coexistence free energy ϕ^{coex} of the athermal ($\varepsilon^* = 0$) C* phase as a function of ζ for different values of λ . The points correspond to those shown in Figs. 9, 10, and S3. Errors estimated to be < 0.05.

Figure 12 summarizes the $\lambda - \zeta$ conditions at which the athermal I-C* phase coexistence was observed in our simulations. This athermal parameter space is enclosed by a tentative gray area akin to the target region depicted in Figure 4. We observed that the athermal phase transition is restricted to high values of the indentation diameter. Size ratios ζ smaller than 1.23 did not stabilize the athermal C* phase even for $\lambda > 0.9$, while larger than 1.35 ratios destabilized the I phase for $\lambda = 0.9$. These results and the gray region in Fig. 12 are roughly consistent with the combination of ζ - λ values for which our non-additive mixing parameter Δv is negative (see pink-shaded region in Fig. 3). For $\lambda \leq 0.8$, certain combinations of λ and ζ outside the gray region generated a coexistence between the C* and another crystalline phase. Selected results and analysis about this outer area of the phase diagram are provided in the supplementary information.

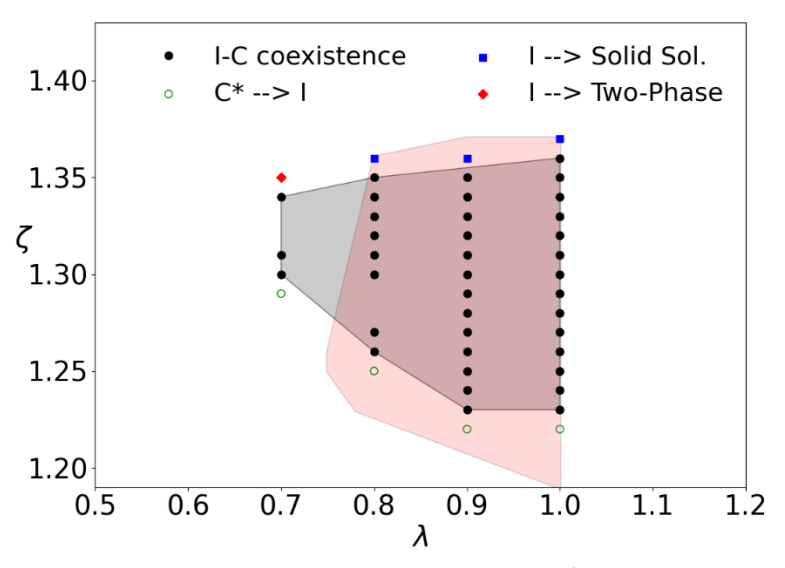


Figure 12 ζ-λ region (shaded in gray and black dots) where athermal (ε* = 0) I-C* phase behavior occurred in our simulations. Points outside this athermal boundary are marked by the phase transformation observed: C*→ I (C* phase melted), I → Solid Sol. (I phase became a substitutionally disorder solid), and I → Two-Phase (I phase separated into sphere-rich crystal + cube-rich crystal). Pink shaded region corresponds to negative values of nonadditive mixing parameter Δν calculated as per Eq. (7).

4. CONCLUSIONS

We studied the I-C* phase transition of spheres and non-convex dimpled cubes to elucidate the effect of varying non-convexity and hence varying degrees of component nonadditivity. We used a known and previously studied system of convex (flat-faced) cubes and spheres as a testbed since these mixtures can form a substitutionally ordered C* phase when energetic attractions (characterized by a well-depth parameter ε^*) are present. Using this as a reference system, we mapped the progression in phase behavior as we increased the size λ of the indentation of the cubes by using the FENEX method. This method can trace coexistence properties by thermodynamic integration along a single variable using polynomial models to fit free-energy data. We used the point $\lambda = 0$ and $\varepsilon^* = 0.55$, $\zeta = 1.23$ as a starting state to obtain coexistence curves for different non-convexity ratios ($\lambda > 0$) of the cubes. We also performed structural analyses to ensure that the states being mapped corresponded to coexistence conditions between the I and C* phase.

The integration carried at fixed ε^* and ζ for increasing value of λ showed that the presence of concave regions on the cubes results in lower coexistence free-energies and pressures (noting that pressure is the main knob used to drive the C*-phase efficient packing), these trends indicate that the indentation helped to stabilize the crystal phase. Furthermore, multiple coexistence lines were estimated for different λ s to find out a crossover value of the concavity that would render the cubesphere energetic attractions unnecessary to form the C* phase. For a fixed $\zeta = 1.23$, that crossover value was $\lambda = 0.9$, which suggests that high non-convexity ratios are necessary to enact a strong entropic bond. Another effect of the cube indentation was that the C* phase had fewer defects and stronger orientational order for higher values of λ . We further conducted integrations over the sphere-to-cube size ratio ζ and λ to outline the region in the $\lambda - \zeta$ design space where athermal I-

C* phase coexistence is attainable, showing that the viable ζ range narrows as λ decreases down to $\lambda = 0.7$. We also found that certain combinations of λ and ζ led to states where congruent melting no longer occurs as another phase outcompeted the I phase for coexistence with the C* phase.

In general, these results show that one can tune the strength of the inter-species entropic bonds to favor ordered phases by adjusting either the size of the concavity on the polyhedral facets or the relative sphere-to-cube ratio. Similar studies of mixtures of spheres and other types of indented polyhedra, like octahedra and dodecahedra, can probe the effect of different NP "valence" (i.e., facets per polyhedron) on the nonadditivity effect of other crystalline compounds. Indeed, some of these types of concave cubical, 61,62 octahedral and dodecahedral frames 63,64 have already been synthesized experimentally. Hence, NPs such as these could be used to try to realize experimentally the congruent phase behavior predicted by simulations. Additionally, the squarewell potential used here describes the energetic interactions simplistically because the focus was on the entropic effect of the cube dimples. For future work, we can improve the description of DNA-mediate-interactions with more detailed representations, such as distance-dependent interparticle contact energies and polybead models, ^{57,65} to identify more subtle multi-body effects on the phase behavior. Beyond thermodynamic stability, it would be interesting to identify design parameters and conditions that lead to robust $I \leftrightarrow C^*$ phase-transition kinetic pathways.⁶⁵ Simulation work along these lines is currently underway.

SUPPLEMENTARY MATERIAL

See supplementary material for additional snapshots of the C* phase and I-C* phase coexistence data for different conditions

ACKNOWLEDGMENTS

Funding support from NSF award CBET-1907369 is gratefully acknowledged. I.Q.M. also acknowledges support from the 2019 SIGHPC Intel Computational & Data Sci. Fellowship.

Statement of Data Availability:

The data that support the findings of this study are available from the corresponding author upon reasonable request.

REFERENCES

- ¹ E.C.M. Vermolen, A. Kuijk, L.C. Filion, M. Hermes, J.H.J. Thijssen, M. Dijkstra, and A. van Blaaderen, Proc. of the Natl. Acad. of Sci.s of the United States of America **106**, 16063 (2009).
- ² T. Hanrath, J. of Vacuum Sci. & Technology A: Vacuum, Surfaces, and Films **30**, 030802 (2012).
- ³ X.W. Lou, C. Yuan, Q. Zhang, and L.A. Archer, Angewandte Chemie Int.Natl. Ed. **45**, 3825 (2006).
- ⁴ C. Salzemann, I. Lisiecki, A. Brioude, J. Urban, and M.P. Pileni, J. Phys. Chem. B **108**, 13242 (2004).
- ⁵ C. Knorowski and A. Travesset, J. Am. Chem. Soc. **136**, 653 (2014).
- ⁶ F.A. Escobedo, Soft Matter **10**, 8388 (2014).
- ⁷ E. Sanz, C. Valeriani, D. Frenkel, and M. Dijkstra, Phys. Rev. Lett. **99**, 055501 (2007).
- ⁸ M. Girard, J.A. Millan, and M. Olvera de la Cruz, Annual Rev. of Materials Research **47**, 33 (2017).
- ⁹ F.A. Escobedo, J. Chem. Phys. **147**, 214501 (2017).
- ¹⁰ J.E. Condon and A. Jayaraman, Soft Matter **13**, 6770 (2017).
- ¹¹ F. Lu, K.G. Yager, Y. Zhang, H. Xin, and O. Gang, Nature Comm. **6**, 6912 (2015).

- ¹² M. Girard, S. Wang, J.S. Du, A. Das, Z. Huang, V.P. Dravid, B. Lee, C.A. Mirkin, and M.O. de la Cruz, Sci. **364**, 1174 (2019).
- ¹³ R.T. Scarlett, M.T. Ung, J.C. Crocker, and T. Sinno, Soft Matter 7, 1912 (2011).
- ¹⁴ C. Avendaño and F.A. Escobedo, Current Opinion in Colloid and Interface Sci. **30**, 62 (2017).
- ¹⁵ F.A. Escobedo, J. Chem. Phys. **140**, 094102 (2014).
- ¹⁶ M.R. Khadilkar, U. Agarwal, and F.A. Escobedo, Soft Matter **9**, 11557 (2013).
- ¹⁷ F.A. Escobedo, J. Chem. Phys. **146**, 134508 (2017).
- ¹⁸ C. Avendaño and F.A. Escobedo, Soft Matter **8**, 4675 (2012).
- ¹⁹ U. Agarwal and F.A. Escobedo, Nature Materials **10**, 230 (2011).
- ²⁰ S. Torquato and Y. Jiao, Phys. Rev. E **81**, 041310 (2010).
- ²¹ P.F. Damasceno, M. Engel, and S.C. Glotzer, ACS Nano 6, 609 (2012).
- ²² G. van Anders, N.K. Ahmed, R. Smith, M. Engel, and S.C. Glotzer, ACS Nano 8, 931 (2014).
- ²³ E.R. Chen, M. Engel, and S.C. Glotzer, Discrete and Computational Geometry 44, 253 (2010).
- ²⁴ J. de Graaf, R. van Roij, and M. Dijkstra, Phys. Rev. Lett. **107**, 15501 (2011).
- ²⁵ C. Avendaño, G. Jackson, and H.H. Wensink, Molecular Phys. **116**, 2901 (2018).
- ²⁶ C. Chen, Y. Kang, Z. Huo, Z. Zhu, W. Huang, H.L. Xin, J.D. Snyder, D. Li, J.A. Herron, M. Mavrikakis, M. Chi, K.L. More, Y. Li, N.M. Markovic, G.A. Somorjai, P. Yang, and V.R. Stamenkovic, Sci. **343**, 1339 (2014).
- ²⁷ M. Zhao, Z.D. Hood, M. Vara, K.D. Gilroy, M. Chi, and Y. Xia, ACS Nano 13, 7241 (2019).
- ²⁸ S. Yoo, J. Kim, S. Choi, D. Park, and S. Park, Nature Comm. **10**, 5789 (2019).
- ²⁹ H.H. Wensink, V. Kantsler, R.E. Goldstein, and J. Dunkel, Phys. Rev. E Statistical, Nonlinear, and Soft Matter Phys. **89**, 010302 (2014).
- ³⁰ B. Yu, Q. Yang, H. Li, Z. Liu, X. Huang, Y. Wang, and H. Chen, J. of Colloid and Interface Sci. **533**, 304 (2019).
- ³¹ A. Castelli, J. de Graaf, S. Marras, R. Brescia, L. Goldoni, L. Manna, and M.P. Arciniegas, Nature Comm. **9**, 1141 (2018).
- ³² B. Zhao, D. Li, Y. Long, and K. Song, Scientific Reports **9**, 8591 (2019).
- ³³ Z. Zhang, A.S. Keys, T. Chen, and S.C. Glotzer, Langmuir **21**, 11547 (2005).
- ³⁴ J.R. Wolters, G. Avvisati, F. Hagemans, T. Vissers, D.J. Kraft, M. Dijkstra, and W.K. Kegel, Soft Matter **11**, 1067 (2015).

- ³⁵ Y. Wang, Y. Wang, X. Zheng, G.R. Yi, S. Sacanna, D.J. Pine, and M. Weck, J. Am. Chem. Soc. **136**, 6866 (2014).
- ³⁶ D.J. Ashton, R.L. Jack, and N.B. Wilding, Phys. Rev. Lett. **114**, 084907 (2015).
- ³⁷ H.M. Jaeger, Soft Matter **11**, 12 (2015).
- ³⁸ S. Sacanna, W.T.M. Irvine, P.M. Chaikin, and D.J. Pine, Nature **464**, 575 (2010).
- ³⁹ M. Marechal, R.J. Kortschot, A.F. Demirörs, A. Imhof, and M. Dijkstra, Nano Lett. **10**, 1907 (2010).
- ⁴⁰ G. Odriozola and M. Lozada-Cassou, J. Phys. Chem. B **120**, 5966 (2016).
- ⁴¹ B. Widom and J.S. Rowlinson, J. Chem. Phys. **52**, 1670 (1970).
- ⁴² S. Asakura and F. Oosawa, J. Chem. Phys. **22**, 1255 (1954).
- ⁴³ B.W. Holland, Transactions of the Faraday Soc. **61**, 555 (1965).
- ⁴⁴ E. Bergmann, Molecular Phys. **32**, 237 (1976).
- ⁴⁵ W.T. Góźdź*góź and G. Góźdź*, Langmuir **33**, 55 (2017).
- ⁴⁶ A. Kumar and V. Molinero, J. Phys. Chem. Lett. **8**, 5053 (2017).
- ⁴⁷ W. Liu, M. Tagawa, H.L. Xin, T. Wang, H. Emamy, H. Li, K.G. Yager, F.W. Starr, A. v. Tkachenko, and O. Gang, Sci. **351**, 582 (2016).
- ⁴⁸ X. Cottin and P.A. Monson, J. Chem. Phys. **102**, 3354 (1995).
- ⁴⁹ M. Matsuoka, Bunri Gijutsu, Separation Process Engineering 7, 245 (1977).
- ⁵⁰ S. Punnathanam and P.A. Monson, J. Chem. Phys. **125**, 024508(2006).
- ⁵¹ J. Arvo, *Graphic Gems*, (Academic Press Professional, Inc., San Diego, CA, 1990).
- ⁵² S. Gottschalk, M.C. Lin, and D. Manocha, in *Proc. of the 23rd Annual Conference on Computer Graphics and Interactive Techniques, SIGGRAPH 1996* (Association for Computing Machinery, Inc, 1996), pp. 171–180.
- ⁵³ M. Mehta and D.A. Kofke, Chem. Eng. Sci. **49**, 2633 (1994).
- ⁵⁴ M.R. Shirts and J.D. Chodera, J. Chem. Phys. **129**, 124105 (2008).
- ⁵⁵ C.H. Bennett, J. Comput. Phys. **22**, 245 (1976).
- ⁵⁶ S. Kumar, J.M. Rosenberg, D. Bouzida, R.H. Swendsen, and P.A. Kollman, J. Comput. Chem. **13**, 1011 (1992).
- ⁵⁷ M. Khaldikar and F.A. Escobedo, J. Chem. Phys. **137**, 194907 (2012).
- ⁵⁸ V. Thapar and F.A. Escobedo, *J. Chem. Phys.* **141**, 124117 (2014).
- ⁵⁹ B.S. John, C. Juhlin, and F.A. Escobedo, J. Chem. Phys. **128**, 044909 (2008).

- ⁶⁰ Y. Xiong, Y. Yang, H. Joress, E. Padgett, U. Gupta, V. Yarlagadda, D.N. Agyeman-Budu, X. Huang, T.E. Moylan, R. Zeng, A. Kongkanand, F.A. Escobedo, J.D. Brock, F.J. DiSalvo, D.A. Muller, and H.D. Abruña, Proc. Natl. Acad.Sci.s of the United States of America **116**, 1974 (2019).
- ⁶¹ C.W. Yang, K. Chanda, P.H. Lin, Y.N. Wang, C.W. Liao, and M.H. Huang, J. Am. Chem. Soc. **133**, 19993 (2011).
- ⁶² M. Jin, H. Zhang, Z. Xie, and Y. Xia, Angewandte Chemie Int. Ed. **50**, 7850 (2011).
- ⁶³ Y. Tian, Y. Zhang, T. Wang, H.L. Xin, H. Li, and O. Gang, Nature Materials **15**, 654 (2016).
- ⁶⁴ K. Ma, Y. Gong, T. Aubert, M.Z. Turker, T. Kao, P.C. Doerschuk, and U. Wiesner, Nature **558**, 577 (2018).
- ⁶⁵ F. A. Escobedo, J. Chem. Phys. **145**, 211903 (2016).